
Article:
Chen, M., Liu, D., Li, W. et al. (11 more authors) (2019) Influences of non-fullerene acceptor fluorination on three-dimensional morphology and photovoltaic properties of organic solar cells. ACS Applied Materials & Interfaces, 11 (29). pp. 26194-26203. ISSN 1944-8244

https://doi.org/10.1021/acsami.9b07317

Influences of non-fullerene acceptor fluorination on three-dimensional morphology and photovoltaic properties of organic solar cells

Mengxue Chen[1,2], Dan Liu[1,2], Wei Li[1,2], Robert S. Gurney[1,2], Donghui Li[1,2], Jinlong Cai[1,2], Emma L. K. Spooner[3], Rachel C. Kilbride[3], James D. McGettrick[4], Trystan M. Watson[4], Zhe Li[5], Richard A. L. Jones[3], David G. Lidzey[3], Tao Wang[1,2]*

[1]School of Materials Science and Engineering, Wuhan University of Technology, Wuhan 430070, China E-mail: twang@whut.edu.cn

[2]State Key Laboratory of Silicate Materials for Architectures, Wuhan University of Technology, Wuhan, 430070, China

[3]Department of Physics and Astronomy, University of Sheffield, Sheffield, S3 7RH, UK

[4]SPECIFIC, College of Engineering, Bay Campus, Swansea University, Swansea, SA1 8EN, UK

[5]School of Engineering, Cardiff University, Cardiff, Wales UK, CF24 3AA

Abstract: Fluorination of conjugated molecules has been established as an effective structural modification strategy to influence properties, and has attracted extensive attention in organic solar cells (OSCs). Here, we have investigated optoelectronic and photovoltaic property changes of OSCs made of polymer donors with the non-fullerene acceptors (NFAs) ITIC and IEICO and their fluorinated counterparts IT-4F and IEICO-4F. Device studies show that fluorinated NFAs lead to reduced V_{oc} but increased J_{sc} and FF, and therefore the ultimate influence to efficiency depends on the compensation of V_{oc} loss and gains of J_{sc} and FF. Fluorination lowers energy levels of NFAs, reduces their electronic bandgaps and red-shifts the absorption spectra. The impact of fluorination on the molecular order depends on the specific NFA, with the conversion of ITIC to IT-4F reduces structural order, which can be reversed after blending with the donor PBDB-T. Contrastingly, IEICO-4F presents stronger π–π stacking after fluorination from IEICO, and this is further strengthened after blending with the donor PTB7-Th. The photovoltaic blends universally present a donor-rich surface region which can promote charge transport and collection towards anode in inverted OSCs. The fluorination of NFAs, however, reduces the fraction of donors in this donor-rich region, consequently encourage the intermixing of donor/acceptor for efficient charge generation.

Key words: organic solar cells; non-fullerene acceptors; fluorination; three-dimensional morphology; photovoltaic properties

Introduction

As a promising renewable energy generation source, organic solar cells (OSCs) have attracted wide attention due to their tunable optoelectronic properties, solution and low-cost fabrication, mechanical flexibility, and semi-transparence.[1-11] The power conversion efficiency (PCE) of binary single-junction OSCs has been boosted to over 16%[12] through designing new photovoltaic materials, constructing favorable device architecture and optimizing the nanoscale morphology within the photoactive layer.[13-18]

Over the past 4 years, the breakthroughs in design and synthesis of a series of non-fullerene acceptors (NFAs) have opened up a new landscape for OSCs.[14, 19-23] NFAs usually comprise of an acceptor–donor–acceptor (A–D–A) structure, where an electron-donating unit (D) constitutes the core and electron-deficient groups (A) serve as terminal moieties.[24-27] Compared with fullerene derivative acceptors, NFAs show a multitude of advantages including tunable energy levels, strong absorption in the visible and near-infrared region, as well as high carrier mobility.[28] For example, Zhan *et al.* reported an NFA ITIC based on a bulky seven-ring fused core (indacenodithieno[3, 2-b]thiophene, IDT) having four 4-hexylphenyl substitutions and terminated with 2-(3-oxo-2,3-dihydroinden-1-ylidene)malononitrile (INCN) groups,[29] which delivered a maximum PCE of 11.2% with PBDB-T serving as the electron donor.[30] Hou *et al.* reported another IDT-based NFA named IEICO, which gave a maximum PCE of 8.4% when PTB7-Th was employed as the donor.[31]

To further improve the efficiency of non-fullerene OSCs, the introduction of fluorine (F) atoms into NFAs has been widely investigated.[32-38] The F atom is an electronegative element with a van der Waals radius of 147 pm only, being 20% larger compared to a radius of 120 pm of the hydrogen atom.[39] After substituting F atoms on the terminal blocks of ITIC, the new NFA IT-4F shows a reduced optical bandgap and downshifted energy levels. As a result, the IT-4F-based OSCs delivered a maximum PCE of 13.1% with PBDB-T-SF as the donor and 13.5% with PM6 as the donor.[40, 41] Using this same strategy, IEICO-4F emerged from IEICO, whose bandgap is reduced to 1.24 eV as a result of the enhanced intramolecular charge transfer effect, and the PCE of the PBT7-Th:IEICO-4F binary OSC reached 10.0%.[42]

Whilst the effect of fluorination on the optical absorption and energy levels of NFAs has been well explored, its effects on the molecular order and aggregation in photovoltaic blends are rarely

investigated. The nanoscale morphology, from molecular and aggregation levels, plays a critical role in determining PCE of OSCs in both lateral and vertical directions of the photoactive layers.[43-45] Unraveling the effects of fluorination on these structural features and understanding the underlying mechanisms can facilitate the precise control of the nanoscale morphology and enable a rational design of device architecture to optimize performance. In this work, we have applied synchrotron-based grazing incidence wide-angle X-ray scattering (GIWAXS), surface energy analysis and X-ray photoelectron spectroscopy (XPS) depth profiles, to investigate the three-dimensional morphology of PBDB-T:IT-4F and PTB7-Th:IEICO-4F photovoltaic films, with PBDB-T:ITIC and PTB7-Th:IEICO films serving as control samples. The three-dimensional morphology is correlated with photovoltaic properties of OSCs to illuminate the comprehensive influences of fluorination. We demonstrate that the impacts of fluorination on the molecular ordering depend on the specific NFA, but fluorination increases donor/acceptor mixing for efficient charge generation by decreasing the enrichment of donors near film surface, whilst still maintain a favorable donor-rich region near the anode for effective extraction in inverted OSCs.

Results and Discussion

Device performance

The chemical structures and energy levels of electron donors (PBDB-T, PTB7-Th) and NFAs (ITIC, IT-4F, IEICO, IEICO-4F) investigated in this work are shown in **Figure 1a, b**. The highest occupied molecular orbital (HOMO) and the lowest unoccupied molecular orbital (LUMO) levels of ITIC and IEICO are -5.48/-3.83 eV and -5.32/-3.95 eV, respectively. Their fluorinated counterparts IT-4F and IEICO-4F show lowered HOMO/LUMO levels, being -5.66/-4.14 eV and -5.44/-4.19 eV, due to the strong electron-withdrawing ability of F atoms which enhanced the push-pull effect between the core unit and the terminal groups.[30, 32, 40, 42] Fluorination therefore reduces the electronic bandgap of NFAs. The absorption spectra of these pure NFA films are presented in **Figure 1c**. The ITIC film shows a primary absorption peak at around 703 nm, and the IEICO film presents a primary peak at around 802 nm. After fluorination, these absorption spectra red-shift, with the primary peaks of IT-4F and IEICO-4F films located at 723 and 865 nm respectively. The pure PBDB-T film displays absorption peaks at 584 and 622 nm, and the pure PTB7-Th film absorbs light at longer wavelengths (see **Figure S1c**). Previous work has

demonstrated that PBDB-T matches ITIC better, and PTB7-Th works with IEICO more effectively.[31, 32]

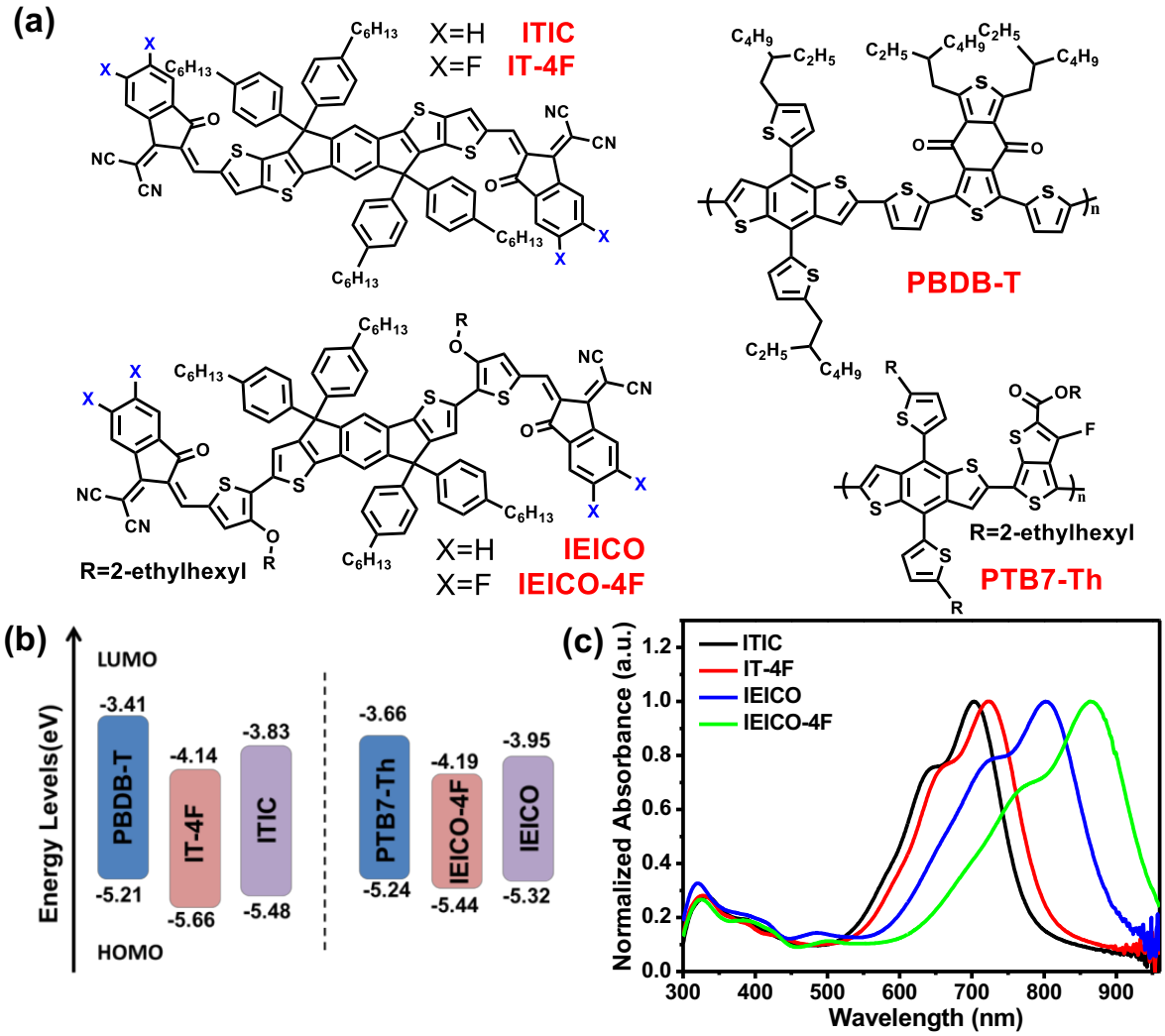

Figure 1 (a) Chemical structures and (b) Energy level alignments of donors (PBDB-T, PTB7-Th) and acceptors (IT-4F/ITIC, IEICO-4F/IEICO). (c) Normalized absorbance of ITIC, IT-4F, IEICO and IEICO-4F films.

In order to investigate the effects of fluorination of ITIC and IEICO on device performance, we fabricated OSCs in an inverted configuration by spin casting the donor:acceptor solution at their optimum blending ratios (1:1 w/w for PBDB-T:ITIC/IT-4F and 1:1.5 w/w for PTB7-Th:IEICO/IEICO-4F respectively) on a ZnO electron-transport layer (ETL), followed by applying a MoO_3/Ag bilayer via thermal evaporation under high vacuum. Previous work[30, 31, 41, 42] also proved that the addition of 1,8-diiodooctane (DIO) and subsequent thermal annealing (TA) help to improve the device efficiency of OSCs, and we therefore adopted this recipe to make devices with high efficiency. The J-V curves of our best-performing OSCs with different

photoactive layers are displayed in **Figure 2a**, with the device metrics summarized in **Table 1**. When ITIC served as the electron acceptor, the PBDB-T:ITIC OSC gave a maximum PCE (PCE_{max}) of 11.2%, with a fill-factor (FF) of 72.5%, a short-circuit current density (J_{sc}) of 17.1 mA cm^{-2} and an open-circuit voltage (V_{oc}) of 0.91 V. By contrast, the fluorination of ITIC (*i.e.* IT-4F) helped increase the J_{sc} to 19.4 mA cm^{-2} and FF to 73.1%. However, the V_{oc} was substantially reduced to 0.67 V, leading to a reduced PCE_{max} of 9.6%. Previous work has demonstrated that one of the key design principles to minimize voltage losses, *i.e.* to get high V_{oc}, is to permit a low energy offset between donor and acceptor.[46] The energy offset, $\Delta E_{LUMO}=D_{LUMO}-A_{LUMO}$ increases from 0.42 eV of PBDB-T:ITIC device to 0.73 eV of PBDB-T:IT-4F device, a value that is excessive for exciton dissociation and deteriorates the device V_{oc} from 0.91 V to 0.67 V. As shown in **Figure S1** and **Table S1**, when using PBDB-T-2F (HOMO/LUMO=-5.48/-3.64 eV)[47] as the electron donor to reduce the energy offset with IT-4F (ΔE_{LUMO}=0.5 eV), V_{oc} can be increased from 0.67 to 0.85 V, leading to a remarkable PCE_{max} of 13.1%. After fluorination, the changes in device metrics of PTB7-Th:IEICO-4F OSC fellow previous trends. The V_{oc} was again found reduced from 0.90 to 0.72 eV. The difference in this case is that the huge improvements of FF (from 59.4 to 67.0 %) and J_{sc} (from 12.5 to 22.1 mA cm^{-2}) compensate for the V_{oc} loss, and result in an improved PCE_{max} from 6.7 to 10.7%.

To verify the accuracy of the J-V measurements, the corresponding external quantum efficiencies (EQE) of various devices were measured and are shown in **Figure 2b**. The J_{sc} values integrated from the EQE spectra (see **Table 1**) are only *ca.* 7% less than that those obtained from J-V scans, therefore confirming the reliability of our J-V measurements. The EQE spectrum illustrated that the PBDB-T:ITIC device responded in the wavelength range from 300 to 800 nm, and the EQE spectrum extended to 850 nm when using IT-4F as the acceptor. The intensity of the EQE spectrum was increased between 700 to 850 nm, which is presumably due to the light absorption of IT-4F in this spectrum range, leading to slightly increased device J_{sc}. The fact that the EQE spectrum was reduced marginally in the wavelength range from 300 to 700 nm suggests that the nanoscale morphology in PBDB-T:IT-4F was not superior for charge generation and collection compared to that of the PBDB-T:ITIC system. The EQE spectrum of PTB7-Th:IEICO OSC exhibited a broader spectral response ranging from 300 to 900 nm, and was further extended to 1000 nm when replacing IEICO with IEICO-4F. Notably, the intensity of the EQE spectrum was

significantly improved in the whole wavelength range from 300 to 1000 nm, and we attribute this to both the larger energy offset and optimized nanoscale morphology in PTB7-Th:IEICO-4F that facilitate charge generation and collection.

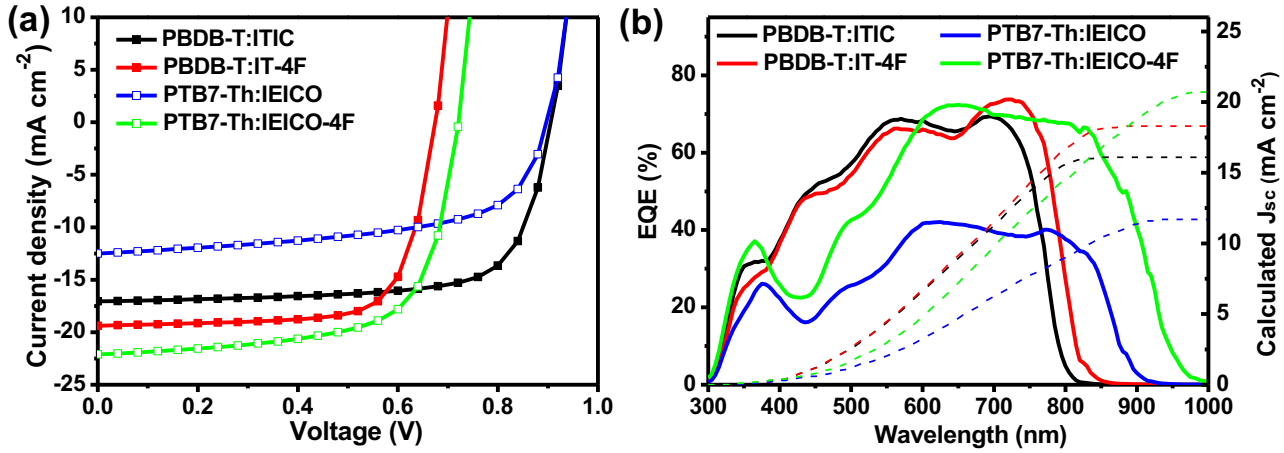

Figure 2 (a) J-V characteristics, (b) EQE spectra of PBDB-T:ITIC, PBDB-T:IT-4F, PTB7-Th:IEICO and PTB7-Th:IEICO-4F OSCs.

Table 1 Photovoltaic parameters of OSCs measured at an illumination of AM 1.5 G, 100 mW cm^{-2}. The average PCE values and standard deviations were obtained from over 15 individual devices.

Donor:Acceptor	FF	J_{sc}	Calculated J_{sc}	V_{oc}	PCE_{max} (PCE_{avg})
	[%]	[mA cm^{-2}]	[mA cm^{-2}]	[V]	[%]
PBDB-T:ITIC	72.5	17.1	16.1	0.91	11.2 (10.9±0.4)
PBDB-T:IT-4F	73.1	19.4	18.4	0.67	9.6 (9.2±0.5)
PTB7-Th:IEICO	59.4	12.5	11.7	0.90	6.7 (6.0±0.9)
PTB7-Th:IEICO-4F	67.0	22.1	20.8	0.72	10.7 (10.3±0.6)

Molecular ordering

We continued to explore the nanoscale morphology in these various photovoltaic blends to illustrate how the microstructure will affect the photovoltaic properties. We first gained insight into the lateral morphology related to molecular order and phase-separation between donors and acceptors. The molecular packing characteristics of the pure and blend films were investigated by GIWAXS. The 2D GIWAXS patterns and 1D out-of-plane (OOP) and in-plane (IP) profiles of these films are shown in **Figures 3** and **4**. Previous GIWAXS measurements have shown that pure PBDB-T presents the (100) lamellar diffraction peak at q=0.26 $Å^{-1}$ and the (010) π–π stacking peak

at q=1.70 Å^{-1}, in both out-of-plane and in-plane directions, indicating the presence of both face-on and edge-on molecular orientations.[48] In **Figure 3a**, the broad diffraction peak at q_z=1.52 Å^{-1} originates from the face-on π–π stacking of ITIC with a stacking distance of 4.1 Å (d=2π/q), consistent with previously reported values.[49] The weak diffraction peaks at q_{xy}=0.34, 0.42 and 0.82 Å^{-1} in the IP profile were indexed as (001) backbone peak, and (100) and (200) lamellar stacking respectively. Moreover, ITIC also exhibited bimodal lamellar stacking in both face-on and edge-on directions, which is evidenced by the appearance of diffraction peaks at both q_z=0.48 Å^{-1} and q_{xy}=0.42 Å^{-1}. The edge-on lamellar stacking is therefore tighter in the OOP direction (d=13.1 Å) than that in the IP direction (d=15.0 Å). After fluorination, neat IT-4F film showed reduced structural ordering, where no well-defined diffraction peaks were recorded (see **Figure 3b**), and this observation is consistent with literature reports.[41] After mixing ITIC with PBDB-T, the original (100) lamellar peaks as well as the (010) π–π stacking peaks of ITIC and PBDB-T both appeared without obvious changes. After mixing IT-4F with PBDB-T, the blend film showed a π–π stacking peak at q_z=1.70 Å^{-1} that is associated with PBDB-T. However, a new diffraction peak locating at q_z=0.38 Å^{-1} emerged and can be defined as the (100) lamellar stacking of IT-4F. Thus, the fluorination of ITIC to IT-4F greatly reduces the structural ordering, which can be reversed after blending with the donor PBDB-T.

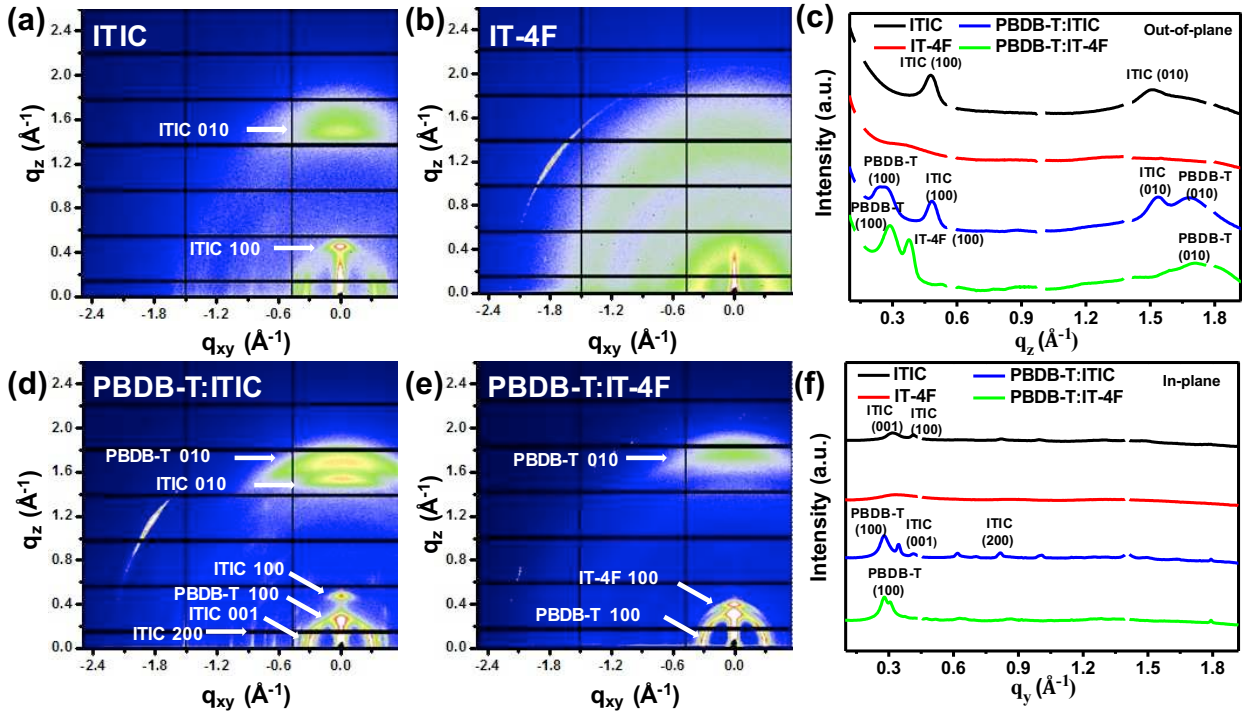

Figure 3 2D GIWAXS of (a) pure ITIC film, (b) pure IT-4F film, (d) PBDB-T:ITIC blend film and

(e) PBDB-T:IT-4F blend film. (c) Out-of-plane and (f) in-plane 1D profiles of these films.

For the pure IEICO film, the diffraction peaks located at q_{xy}=0.31 Å^{-1} and q_z=1.80 Å^{-1} were indexed as the (100) and (010) peaks, corresponding to the lamellar stacking in the IP direction and π–π stacking in the OOP direction. Similar phenomena could be observed in the pure IEICO-4F film (with peaks at q_{xy}=0.29 Å^{-1} and q_z=1.82 Å^{-1}), suggesting structural order in both IEICO and IEICO-4F were preferentially face-on oriented. **Figure 4a-c** shows that IEICO-4F presented stronger π–π stacking after fluorination.[50] After blending them with the donor PTB7-Th, abnormal structural order changes were observed. It is commonly seen that the similar chemical structures of polymer donors and NFAs usually resulted in intimate mixing to reduce molecular ordering. Shown in **Figure 4c**, a number of additional rings ranging from 0.5 Å^{-1} to 1.5 Å^{-1} appear in the PTB7-Th:IEICO blend film, with the backbone diffraction peak (001) of IEICO emerged. The presence of these additional diffraction peaks suggests highly enhanced crystallization of IEICO in the blend. Similar observations can be found in the PTB7-Th:IEICO-4F blend film, with the backbone diffraction peak (001) distinguishable in **Figure 4e**. The enhanced ordering of IEICO and IEICO-4F by the donor PTB7-Th are also met by the narrowing of their π–π stacking diffraction peaks. Note here that the fluorination of IEICO didn't alter its predominant face-on orientation.[51]

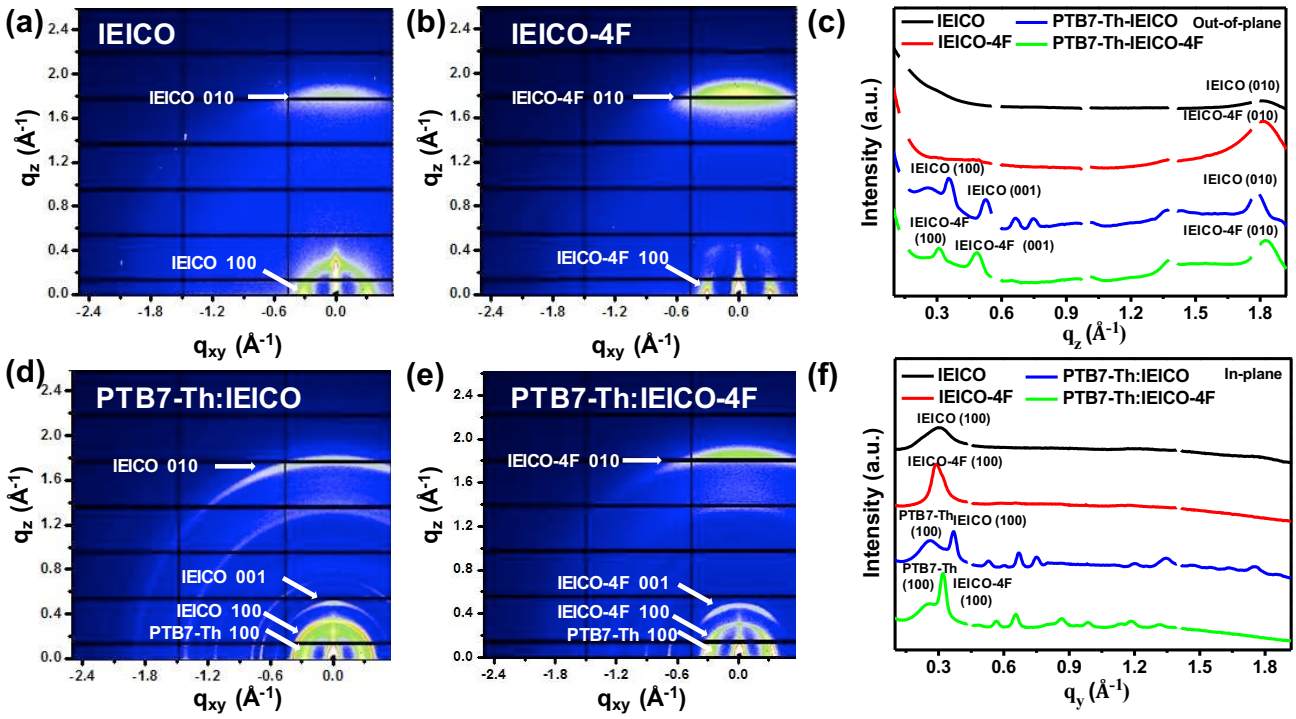

Figure 4 2D GIWAXS of (a) IEICO based-(b) IEICO-4F based- (d) PTB7-Th:IEICO based- and (e) PTB7-Th:IEICO-4F based-films. (c) Out-of-plane and (f) in-plane 1D profiles of these films.

Our GIWAXS investigation supports that the impact of fluorination on the molecular order depends on the specific NFA, with the conversion of ITIC to IT-4F reduces structural order whilst IEICO-4F presents stronger π–π stacking after fluorination from IEICO. Glass transition temperature (T_g) is an indication of intermolecular interactions of organic molecules. We have therefore probed the T_g*s* of neat ITIC, IT-4F, IEICO and IEICO-4F films via spectroscopic ellipsometry. [52,53,54] Contrasting T_g variations are also observed in the two different systems after fluorination, with the T_g of pure IT-4F being reduced to 144 °C from 168 °C of ITIC whilst that of IEICO-4F being increased from 150 °C of IEICO to 157 °C. A higher T_g is associated with stronger π–π stacking intermolecular interactions within ITIC and IEICO-4F, a result that is consistent with the GIWAXS measurements.

Vertical component distribution

The surface morphology of various photovoltaic blends was revealed via atomic force microscopy (AFM) and shown in **Figure S3a-d**. The surfaces of all blend films show at least two phases appearing bright and dark respectively. However, no more information regarding the size of the phase separation as well as the material component on the film surface can be concluded confidently due to the limitation of this characterization technique. We then used XPS with a gas-cluster etching accessory to extract vertical component distributions in photovoltaic blend thin films cast on ZnO substrates. During the analysis of XPS data, nitrogen was used as the characteristic element of acceptors because nitrogen (N) is absent in donors.[55] Taking a PBDB-T:ITIC thin film data as the example, the N (1s) signal represents the content of ITIC, whilst the S (2p) peak represents the total content of PBDB-T and ITIC. Hence, the N (1s)/S (2p) peak-area ratio could be proportionally correlated to the ITIC concentration in the blend. We define here the air interface as thickness 0, and the substrate interface as thickness 1. The ZnO signal starts to appear and its intensity increases abruptly as the etch penetrates further towards the substrate.[45] As shown in **Figure 5a**, **b**, both original and the fluorinated photovoltaic blend films present a donor-rich surface layer. The donor/acceptor ratios of PBDB-T/ITIC and PBDB-T/IT-4F are 3.1 and 1.5 (corresponding to PBDB-T volume contents of 75.6% and 60.0%) respectively. Similar results are se in the PTB7-Th:IEICO blend thin film, where the donor/acceptor ratio at the film surface was 3.8 (corresponding to a PBDB-T volume content of 79.2%). Meanwhile, a donor-rich surface region also present in the PTB7-Th/IEICO-4F blend film, but the ratio reduced dramatically

to 2.6 (corresponding to a PBDB-T volume content of 72.2%). This is a result of the lower surface energies (γ) of polymer donors. The contact angles (θ) and the calculated surface energies of pure donor or acceptor films are presented in **Figure S4**. The surface energies of pure ITIC, IT-4F, IEICO and IEICO-4F films are 29.5, 28.5, 28.2 and 25.3 mN m^{-1} respectively. Fluorination therefore decreases the surface energy of NFAs The surface energies of polymer donors are much lower compared with those of NFAs (22.3 and 21.5 mN m^{-1} for PBDB-T and PTB7-Th respectively), which drive them to migrate upwards the surface region of the blend film during solution casting to minimize the total free energy of the blend system. The reduced surface energy of fluorinated NFAs weakens the vertical stratification, evidenced by the reduced donor/acceptor ratio in the surface region of PBDB-T/IT-4F and PTB7-Th/IEICO-4F.[56] For inverted devices, energy levels between donors (PBDB-T, PTB7-Th) and MoO_3 are closer, thus donor enrichment at the surface is beneficial for charge transport and collection for inverted OSCs.[57] However, excessive enrichment of donors in this region will reduce the intermixing of donors and acceptors, and therefore reduce the interfacial area for exciton dissociation, leading to reduced J_{sc}. Fluorination reduces the fraction of donors in this region (see schematics in **Figure 5c**), therefore facilitates charge generation and the resulting devices have higher J_{sc}, as evidenced by our device study summarized in Table 1. With the progression of XPS etching process to reveal component information in the bulk of the film, the donor/acceptor ratio began to reduce and reach a plateau value of 1 after around 10 nm into the blend film, and kept constant throughout the bulk of the remaining film. Therefore, we can approximately determine that the thickness of surface donor-rich region is 10 nm. We note that this value of surface region can be reported more accurately if the step size of our XPS etching could be reduced further.

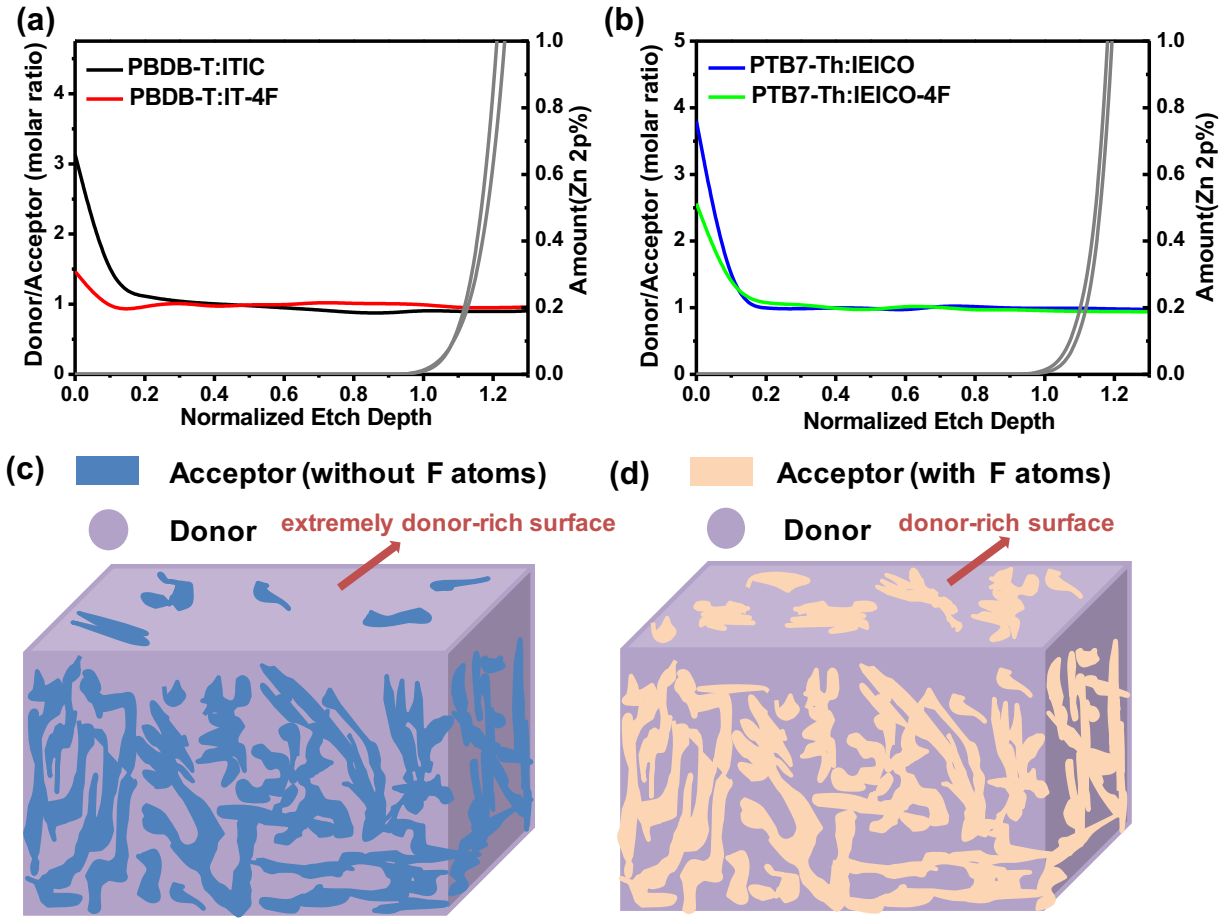

Figure 5 XPS depth profiles of (a) PBDB-T:ITIC-based, PBDB-T:IT-4F-based films and (b) PTB7-Th:IEICO-based, PTB7-Th:IEICO-4F-based films. Normalized etch depth 0 corresponds to the air interface, and depth 1 corresponds to the substrate interface. Schematic of vertical component distribution of photovoltaic blends containing (c) normal NFAs and (d) fluorinated NFAs.

Device physics

The nanoscale morphology in the lateral direction (*i.e.* molecular order, phase separation) mainly influences photocurrent generation and recombination, whilst the vertical component distribution primarily affects charge transport and collection. To assess how the lateral and vertical morphology of the active layer will impact these optoelectronic processes, we have carried out further device physics studies. The exciton dissociation and charge collection processes are evaluated by analyzing the photocurrent (J_{ph}) versus effective voltage (V_{eff}) plots of various devices (**Figure 6a** and **Table 2**). Here, J_{ph} is defined as J_{light}- J_{dark}, where J_{light} and J_{dark} are the photocurrent densities under illumination and in the dark respectively. V_{eff} is defined as $V_{eff} = V_0 - V_a$, where V_0

is the voltage at the point of J_{ph} = 0 and V_a is the applied bias. Here, the J_{ph} of devices at 1 V has been selected as the pseudo-saturation photocurrent (J_{sat}) for equitable comparison. The J_{ph}/J_{sat} values under short-circuit and the maximal power output conditions represent the exciton dissociation efficiency (P_{diss}) and charge collection efficiency (P_{coll}) respectively.[58] It is found that J_{ph} saturates at large V_{eff} and the P_{diss} values are high for all devices, indicating that all devices have efficient exciton generation and charge dissociation. In addition, the P_{coll} values of all IT-4F and IEICO-4F based devices are generally higher than those of ITIC and IEICO based devices, suggesting the favorable vertical component distribution in the photovoltaic layer contributes at least partly to this favorable effect. Dark J-V curves of electron-only and hole-only devices are shown in **Figure S5** and the corresponding electron (μ_e) and hole (μ_h) mobilities are summarized in **Table 2**. The values of μ_e/μ_h are 1.5, 1.0, 0.7 and 1.1 for PBDB-T:ITIC, PBDB-T:IT-4F, PTB7-Th:IEICO and PTB7-Th:IEICO-4F devices, respectively. After fluorination, μ_e and μ_h haven't been significantly improved but the μ_e /μ_h ratio becomes balanced.

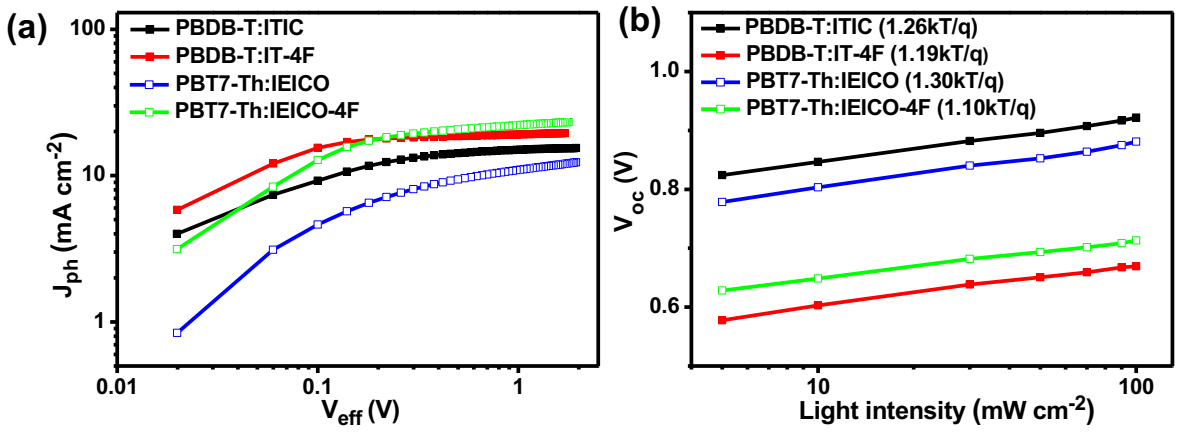

Figure 6 (a) Photocurrent density versus effective voltage curves. (b) V_{oc} versus light intensity of different blend films.

Table 2 J_{sat}, P_{diss}, P_{coll}, charge mobilities and balance of various OSCs.

Donor:Acceptor	J_{sat} [mA cm^{-2}]	P_{diss} [%]	P_{coll} [%]	Hole mobility (μ_e) $cm^2V^{-1}S^{-1}$	Electron mobility (μ_h) $cm^2V^{-1}S^{-1}$	μ_e /μ_h
PBDB-T:ITIC	15.4	99.9	85.8	2.8×10^{-4}	1.9×10^{-4}	1.5
PBDB-T:IT-4F	19.5	99.2	90.4	2.6×10^{-4}	2.7×10^{-4}	1.0
PTB7-Th:IEICO	12.3	99.1	73.0	2.1×10^{-4}	3.1×10^{-4}	0.7
PTB7-Th:IEICO-4F	23.2	98.9	81.5	2.7×10^{-4}	2.5×10^{-4}	1.1

In order to get insight into the charge recombination process in these OSCs, we have evaluated the light intensity dependent V_{oc} changes (**Figure 6b**). Light ideality factor ($n_{id,l}$) values were obtained by $n_{id,l} = \frac{q}{kT} \frac{dV_{oc}}{dln(\Phi)}$, where q is the elementary charge, K is Boltzmann's constant, T is the absolute temperature, and Φ is the fractional light intensity normalized to 1 sun.[59] The $n_{id,l}$ values were 1.26, 1.19, 1.30 and 1.10 for PBDB-T:ITIC, PBDB-T:IT-4F, PTB7-Th:IEICO and PTB7-Th:IEICO-4F devices, respectively. It has been suggested that a unity slope (unit of kT/q) is an indication of bimolecular recombination, while a slope greater than unity suggests that both trap-assisted and bimolecular recombination processes operate in the devices. Therefore, the smaller $n_{id,l}$ values of PBDB-T:IT-4F and PTB7-Th:IEICO-4F devices are indicative of fewer traps. Fluorination of NFAs therefore reduces the trap-assisted recombination.

Table 3 Summary of the electrical parameters of PBDB-T:ITIC, PBDB-T-IT-4F, PTB7-Th:IEICO, and PTB7-Th:IEICO-4F -based OSCs obtained by fitting the Nyquist plots.

Donor:Acceptor	R_s [Ω]	R_1 [Ω]	CPE_1-T [F]	CPE_1-P	R_2 [Ω]	CPE_2-T [F]	CPE_2-P
PBDB-T:ITIC	73.1	50.7	6.5 E^{-9}	0.87	80.9	1.9 E^{-8}	0.95
PBDB-T:IT-4F	85.9	37.9	2.4 E^{-8}	0.92	103.9	2.8 E^{-8}	0.98
PTB7-Th:IEICO	80.5	36.4	1.5 E^{-9}	0.85	165.2	1.2 E^{-8}	0.93
PTB7-Th:IEICO-4F	66.3	24.3	4.2 E^{-9}	0.93	172.1	2.3 E^{-8}	0.99

Figure S6 shows the Nyquist plots of impedance measurements of these devices, from which single characteristic semi-circles are observed. We have applied an equivalent circuit model consisting of three resistances (R_s, R_1 and R_2) and two constant phase elements (CPE_1-T, CPE_2-T) to fit the curves.[58, 60, 61] R_s represents resistance in the device due to numerous electrical contacts and remained largely unchanged for all devices. R_1 represents the transport resistance of the photoactive layer and R_2 corresponds to the recombination resistance of the photoactive layer, both could be used to evaluate carrier transport and recombination processes. The fitted data are summarized in **Table 3**. Values of R_1 (ITIC:50.7Ω, IT-4F:37.9Ω, IEICO:165.2 Ω and IEICO-4F:24.3 Ω) and R_2 (ITIC:80.9Ω, IT-4F:103.9Ω, IEICO: 36.4 Ω and IEICO-4F:172.1 Ω) from this model fitting show that fluorination effectively reduced the transport resistances and increased the recombination resistances. The constant phase element (CPE) is related to the non-ideal

behavior of a capacitor, and is defined by CPE-T and CPE-P. CPE-T represents the capacitance and CPE-P corresponds to the inhomogeneous constant.[58] If CPE-P equals to 1, CPE is an ideal capacitor with the elimination of any defects at the donor:acceptor interface. Our data fitting shows that the CPE-P values of fluorinated NFAs devices increased towards 1, suggesting the interface capacitance between donor and acceptor become more ideal. What's more, the average carrier lifetime (τ) of the photoactive layer can be obtained from the equation: $\tau=R_2\times CPE_2\text{-}T$, and a longer τ suggests a lower recombination rate.[62] The τ values of PBDB-T:IT-4F and PTB7-Th:IEICO-4F OSCs are estimated to be 2.9 and 3.9 μs, higher than those in PBDB-T:ITIC and PTB7-Th:IEICO OXCs (1.5 and 2.0 μs). That is to say, fluorination facilitates charge transport and reduces the recombination rate, which is also evidenced from our measurements of V_{oc} as a function of light intensity. As a result, devices incorporating fluorinated NFAs always show higher J_{sc} and FF, results that agree with our device study shown in the earlier section.

Conclusion

In summary, influences of non-fullerene acceptor fluorination on three-dimensional morphology and photovoltaic properties of OSCs are investigated in this work. Fluorination of NFAs is found to reduce the V_{oc} due to the lowered LUMO and HOMO energy levels and increased energy offset between polymer donors, whilst the J_{sc} and FF will be increased instead due to increased light absorption in the longer wavelength region, as well as improved favorable lateral or vertical morphology for charge separation and collection. The ultimate device efficiency depends on the compensation of loss of V_{oc} and gains of J_{sc} and FF. Therefore the fluorination of ITIC to IT-4F was found to reduce the device PCE from 11.2% to 9.6%, whilst that of IEICO to IEICO-4F was found to increase device PCE from 6.7% to 10.7%. The fluorination of ITIC to IT-4F greatly reduces the structural ordering, which can be improved only after blending with the donor PBDB-T, therefore the nanoscale morphology in PBDB-T:IT-4F is not superior for charge generation and collection compared to that of PBDB-T:ITIC system. Contrastingly, IEICO-4F presents stronger π–π stacking after fluorination from IEICO, and this is further strengthened after blending with the donor PTB7-Th. The polymer:NFA photovoltaic blends universally present an excessive donor-rich surface region before and after the fluorination of NFAs, which can promote charge transport and collection towards anode in inverted OSCs. The fluorination of NFAs however reduces the fraction

of donors in this donor-rich region, consequently enhances the intermixing of donor/acceptor for efficient charge generation.

Experimental Section

Materials: PBDB-T, ITIC, IT-4F, PTB7-Th, IEICO and IEICO-4F were purchased from Solarmer Materials (Beijing) Inc. ZnO precursor solution was prepared following our previous report.[60]

Fabrication of polymer solar cells: Solar cell devices were prepared with an inverted structure. The patterned ITO-glass substrates (resistance ca. 15 Ω per square) were cleaned and treated following our previous report.[57,58,60] The ZnO precursor solution was spin-cast at 4000 r.p.m on the ITO glass, then dried in air for 30 minutes at 200 °C. The photoactive layer was deposited on ZnO surface in a nitrogen-filled glovebox by spin-coating from a 14 mg/mL donor:acceptor solution (1:1 weight ratio for PBDB-T:ITIC/IT-4F and 1:1.5 weight ratio for PTB7-Th:IEICO/IEICO-4F system) with the addition of DIO (0.5 vol% in ITIC-based solution, 0.75 vol% in IT-4F-based solution, 2 vol% in IEICO-based solution and 1 vol% in IEICO-4F-based solution), to obtain films around 100 nm in thickness. After the casting of the photoactive layer, devices were thermally annealed following previous reports. Then, 10 nm MoO_3 and 100 nm Ag were thermally evaporated on the top under high vacuum to finish the device fabrication. The photoactive area is 4 mm^2 defined by the overlapping of anode and cathode.

Characterization: Device J-V characterization was performed under AM 1.5G (100 mW cm^{-2}) simulated sunlight using a 3A solar simulator (Newport, USA) in air at room temperature. Synchrotron grazing incidence wide angle X-ray scattering (GIWAXS) measurements were conducted at beamline I07 of Diamond Light Source in the UK. Film thickness was measured using a spectroscopic ellipsometer (J. A. Woollam, USA). The morphology of film surface was characterized by tapping-mode atomic force microscopy (AFM) (NT-MDT, Russia). Film absorption spectra were obtained using a UV-Visible spectrophotometer (HITACHI, Japan). T_g of thin films was measured via spectroscopic ellipsometry at a heating rate of 3 °C min^{-1}, under a nitrogen flow environment. XPS data were obtained by using a Kratos Axis Supra (Kratos Analytical, Manchester, UK) using a monochromated Al Kα source and depth profiles were obtained via etching with 5 kV Ar_{500}^+ clusters. Water contact angle measurements were carried out using a contact angle measurement system (Attension Theta Lite, Sweden), and the surface energy

was calculated using the equation of state. The light intensity was calibrated using a standard silicon cell that has been previously certified by the National Renewable Energy Laboratory (NREL, USA). J-V curves were recorded using a J-V sweep software (Ossila, UK) and a Keithley 2612B source meter unit. External quantum efficiency (EQE) was performed with an EQE system (Zolix, China). Impedance measurements were measured on an electrochemical workstation (Solartron, U.K.). During the impedance testing, the device was illuminated with a light intensity equal to 0.1 sun and the open circuit voltage was also applied with a small perturbation.

ASSOCIATED CONTENT

Supporting Information

Chemical structure and energy levels of PBDB-T-2F, absorption and J-V curves of PBDB-T-2F:IT-4F OPV; measurements of T_g via spectroscopy ellipsometry; AFM images , water contact angles (θ) , surface energies (γ), electron mobility, hole mobility and impedance spectra of photovoltaic blend films.

Acknowledgments

This work was supported by the National Natural Science Foundation of China (Grants No. 21774097), the Natural Science Foundation of Hubei Province (Grant No. 2018CFA055) and the Fundamental Research Funds for the Central Universities (2019-zy-017). We thank beamline I07 at Diamond Light Source (UK) for providing beam time to perform GIWAXS measurements.

Reference

(1) Heeger, A.J. Semiconducting Polymers: The Third Generation. *Chem. Soc. Rev.* **2010**, *39*, 2354–2371.

(2) Heeger, A.J. Bulk Heterojunction Solar Cells: Understanding the Mechanism of Operation. *Adv. Mater.* **2014**, *26*, 10–28.

(3) Li, G.; Zhu, R.; Yang, Y. Polymer Solar Cells. *Nat. Photonics.* **2012**, *6*, 153–161.

(4) He, Z.; Zhong, C.; Su, S.; Xu, M.; Wu, H.; Cao, Y. Enhanced Power-Conversion Efficiency in Polymer Solar Cells Using an Inverted Device Structure. *Nat. Photonics.* **2012**, *6*, 591–595.

(5) Yip, H.L.; Jen, A.K.Y. Recent Advances in Solution-Processed Interfacial Materials for Efficient and Stable Polymer Solar Cells. *Energy Environ. Sci.* **2012**, *5*, 5994–6011.

(6) Qian, D.; Ye, L.; Zhang, M.; Liang, Y.; Li, L.; Huang, Y.; Guo, X.; Zhang, S.; Tan, Z.; Hou, J. Design, Application, and Morphology Study of a New Photovoltaic Polymer with Strong Aggregation in Solution State. *Macromolecules.* **2012**, *45*, 9611–9617.

(7) He, Z.; Xiao, B.; Liu, F.; Wu, H.; Yang, Y.; Xiao, S.; Wang, C.; Russell, T.P.; Cao, Y. Single-Junction Polymer Solar Cells with High Efficiency and Photovoltage. *Nat. Photonics* **2015**, *9*, 174–179.

(8) Collins, S.D.; Ran, N.A.; Heiber, M.C.; Nguyen, T.Q. Small Is Powerful: Recent Progress in Solution-Processed Small Molecule Solar Cells. *Adv. Energy Mater.* **2017**, *7*, 1602242.

(9) Dai, S.; Zhao, F.; Zhang, Q.; Lau, T. K.; Li, T.; Liu, K.; Ling, Q.; Wang, C.; Lu, X.; You, W.; Zhan, X. Fused Nonacyclic Electron Acceptors for Efficient Polymer Solar Cells. *J. Am. Chem. Soc.* **2017**, *139*, 1336–1343.

(10) Zhu, J.; Ke, Z.; Zhang, Q.; Wang, J.; Dai, S.; Wu, Y.; Xu, Y.; Lin, Y.; Ma, W.; You, W.; Zhan, X. Naphthodithiophene-Based Nonfullerene Acceptor for High-Performance Organic Photovoltaics: Effect of Extended Conjugation. *Adv. Mater.* **2018**, *30*, 1704713.

(11) Liu, W.; Zhang, J.; Zhou, Z.; Zhang, D.; Zhang, Y.; Xu, S.; Zhu, X. Design of a New Fused-Ring Electron Acceptor with Excellent Compatibility to Wide-Bandgap Polymer Donors for High-Performance Organic Photovoltaics. *Adv. Mater.* **2018**, *30*, 1800403.

(12) Fan, B.; Zhang, D.; Li.; M.; Zhong, W.; Zhao, Z.; Ying, Lei.; Huang, F.; Cao, Y. Achieving over 16% efficiency for single-junction organic solar cells. *Sci China Chem*. **2019**, 62, 1-7.

(13) Lopez, S.A.; Sanchez-Lengeling, B.; de Goes Soares, J.; Aspuru-Guzik, A. Design Principles and Top Non-Fullerene Acceptor Candidates for Organic Photovoltaics. *Joule.* **2017**, *1*, 857–870.

(14) Cheng, P.; Li, G.; Zhan, X.; Yang, Y. Next-Generation Organic Photovoltaics Based on Non-Fullerene Acceptors. *Nat. Photonics.* **2018**, *12*, 131–142.

(15) Yang, T.; Cai, W.; Qin, D.; Wang, E.; Lan, L.; Gong, X.; Peng, J.; Cao, Y. Solution-Processed Zinc Oxide Thin Film as a Buffer Layer for Polymer Solar Cells with an Inverted Device Structure. *J. Phys. Chem. C.* **2010**, *114*, 6849–6853.

(16) Kyaw, A.K.K.; Wang, D.H.; Gupta, V.; Zhang, J.; Chand, S.; Bazan, G.C.; Heeger, A.J. Efficient Solution-Processed Small-Molecule Solar Cells with Inverted Structure. *Adv. Mater.* **2013**, *25*, 2397–2402.

(17) Han, G.; Guo, Y.; Ma, X.; Yi, Y. Atomistic Insight Into Donor/Acceptor Interfaces in

High-Efficiency Nonfullerene Organic Solar Cells. *Sol. RRL.* **2018**, *2*, 1800190.

(18) Upama, M.B.; Elumalai, N.K.; Mahmud, M.A.; Wright, M.; Wang, D.; Xu, C.; Uddin, A. Effect of Annealing Dependent Blend Morphology and Dielectric Properties on the Performance and Stability of Non-Fullerene Organic Solar Cells. *Sol. Energy Mater. Sol. Cells.* **2018**, *176*, 109–118.

(19) Holliday, S.; Ashraf, R.S.; Wadsworth, A.; Baran, D.; Yousaf, S.A.; Nielsen, C.B.; Tan, C. H.; Dimitrov, S.D.; Shang, Z.; Gasparini, N.; Alamoudi, M.; Laquai. F.; Brabec, C.J.; Alberto, S.; Durrant, J.R.; McCulloch, I. High-Efficiency and Air-Stable P3HT-Based Polymer Solar Cells with a New Non-Fullerene Acceptor. *Nat. Commun.* **2016**, *7*, 11585.

(20) Yan, C.; Barlow, S.; Wang, Z.; Yan, H.; Jen, A. K. Y.; Marder, S. R.; Zhan, X. Non-Fullerene Acceptors for Organic Solar Cells. *Nature Reviews Materials*. **2018**, *3*, 18003.

(21) Li, S.; Liu, W.; Li, C. Z.; Shi, M.; Chen, H. Efficient Organic Solar Cells with Non-Fullerene Acceptors. *Small*. **2017**, *13*, 1701120.

(22) Xiong, S.; Hu, L.; Hu, L.; Sun, L.; Qin, F.; Liu X.;Fahlman, M.;Zhou, Y. 12.5% Flexible Nonfullerene Solar Cells by Passivating the Chemical Interaction Between the Active Layer and Polymer Interfacial Layer. *Adv. Mater.* **2019**, *31*, 1806616.

(23) Aldrich, T. J.; Swick, S. M.; Melkonyan, F. S.; Marks, T. J. Enhancing Indacenodithiophene Acceptor Crystallinity via Substituent Manipulation Increases Organic Solar Cell Efficiency. *Chem. Mater*. **2017**, *29*, 10294−10298.

(24) Sun, J.; Ma, X.; Zhang, Z.; Yu, J.; Zhou, J.; Yin, X.; Yang, L.; Geng, R.; Zhu, R.; Zhang, F.; Tang, W. Dithieno[3,2-b:2′,3′-d]Pyrrol Fused Nonfullerene Acceptors Enabling Over 13% Efficiency for Organic Solar Cells. *Adv. Mater.* **2018**, *30*, 1707150.

(25) Song, J.; Li, C.; Ye, L.; Koh, C.W.; Cai, Y.; Wei, D.; Woo, H. Y.; Sun, Y. Extension of Indacenodithiophene Backbone Conjugation Enables Efficient Asymmetric A-D-A Type Non-Fullerene Acceptors. *J. Mater. Chem. A*. **2018**, *6*, 18847-18852.

(26) Luo, Z.; Bin, H.; Liu, T.; Zhang, Z. G.; Yang, Y.; Zhong, C.; Qiu, B.; Li, G.; Gao, W.; Xie, D.; Wu, K.; Sun, Y.; Liu, F.; Li, Y.; Yang, C. Fine-Tuning of Molecular Packing and Energy Level through Methyl Substitution Enabling Excellent Small Molecule Acceptors for Nonfullerene Polymer Solar Cells with Efficiency up to 12.54%. *Adv. Mater.* **2018**, *30*, 1706124.

(27) Aldrich, T. J.; Zhu, W.; Mukherjee, S.; Richter, L. J.; Gann, E.; DeLongchamp,D. M.;

Facchetti, A.; Melkonyan, F. S.; Marks, T. J. Stable Postfullerene Solar Cells via Direct C−H Arylation Polymerization: Morphology−Performance Relationships. *Chem. Mater.* **2019**, *31*, 4313−4321.

(28) Chen, W.; Zhang, Q. Recent Progress in Non-Fullerene Small Molecule Acceptors in Organic Solar Cells (OSCs). *Journal of Materials Chemistry C*. **2017**, *5*, 1275-1302.

(29) Lin, Y.; Wang, J.; Zhang, Z. G.; Bai, H.; Li, Y.; Zhu, D.; Zhan, X. An Electron Acceptor Challenging Fullerenes for Efficient Polymer Solar Cells. *Adv. Mater.* **2015**, *27*, 1170–1174.

(30) Zhao, W.; Qian, D.; Zhang, S.; Li, S.; Inganäs, O.; Gao, F.; Hou, J. Fullerene‐Free Polymer Solar Cells with over 11% Efficiency and Excellent Thermal Stability. *Adv. Mater.* **2018**, *28*, 4734-4739.

(31) Yao, H.; Chen, Y.; Qin, Y.; Yu, R.; Cui, Y.; Yang, B.; Li, S.; Zhang, K.; Hou, J. Design and Synthesis of a Low Bandgap Small Molecule Acceptor for Efficient Polymer Solar Cells. *Adv. Mater.* **2016**, *28*, 8283–8287.

(32) Deng, D.; Zhang, Y.; Zhang, J.; Wang, Z.; Zhu, L.; Fang, J.; Xia, B.; Wang, Z.; Lu, K.; Ma, W.; Zhan, X. Fluorination-Enabled Optimal Morphology Leads to over 11% Efficiency for Inverted Small-Molecule Organic Solar Cells. *Nat. Commun.* **2016**, *7*, 13740.

(33) Wang, Z.; Xu, X.; Li, Z.; Feng, K.; Li, K.; Li, Y.; Peng, Q. Solution-Processed Organic Solar Cells with 9.8% Efficiency Based on a New Small Molecule Containing a 2D Fluorinated Benzodithiophene Central Unit. *Adv. Electron. Mater.* **2016**, *2*, 1600061.

(34) Kan, B.; Zhang, Q.; Wan, X.; Ke, X.; Wang, Y.; Feng, H.; Zhang, M.; Chen, Y. Oligothiophene-Based Small Molecules with 3,3′-Difluoro-2,2′-Bithiophene Central Unit for Solution-Processed Organic Solar Cells. *Org. Electron. physics, Mater. Appl.* **2016**, *38*, 172–179.

(35) Lin, Z.; Huang, K.; Wang, Z.; Chen, X.; Sun, J.; Xu, Z.; He, T.; Yin, S.; Li, M.; Zhang, Q.; Q, H. Alkyl Side-Chain and Fluorination Engineering in the Indeno[1,2-b]Fluorene-Based Small-Molecule Acceptors for Efficient Non-Fullerene Organic Solar Cells. *Dye. Pigment.* **2019**, *160*, 432–438.

(36) Song, X.; Gasparini, N.; Nahid, N.; Paleti, S.; Wang, J.; Ade, H.; Baran, D. Dual Sensitizer and Processing-Aid Behavior of Donor Enables Efficient Ternary Organic Solar Cells. *Joule.* **2019**, *3*, 1-12.

(37) Timalsina, A.; Hartnett, P. E.; Melkonyan, F. S.; Strzalka, J.; Reddy, V. S.; Facchetti, A.;

Wasielewski, M. R.; Marks, T. J. New Donor Polymer with Tetrafluorinated Blocks for Enhanced Performance in Perylenediimide-Based Solar Cells. J. Mater. Chem. A. 2017, 5, 5351-5361.

(38) Aldrich, T. J.; Matta, M.; Zhu, W.; Swick, S.M.; Stern,C. L.; Schatz, G. C.; Facchetti, A.; Melkonyan, F. S.; Marks, T. J. Fluorination Effects on Indacenodithienothiophene Acceptor Packing and Electronic Structure, End-Group Redistribution, and Cell Photovoltaic Response. *J. Am. Chem. Soc*. **2019**, *141*, 3274−3287.

(39) Zhang, Q.; Kelly, M. A.; Bauer, N.; You, W. The Curious Case of Fluorination of Conjugated Polymers for Solar Cells. *Acc. Chem. Res.* **2017**, *50*, 2401–2409.

(40) Zhao, W.; Li, S.; Yao, H.; Zhang, S.; Zhang, Y.; Yang, B.; Hou, J. Molecular Optimization Enables over 13% Efficiency in Organic Solar Cells. *J. Am. Chem. Soc.* **2017**, *139*, 7148–7151.

(41) Fan, Q.; Su, W.; Wang, Y.; Guo, B.; Jiang, Y.; Guo, X.; Liu, F.; Russell, T.P.; Zhang, M.; Li, Y. Synergistic Effect of Fluorination on Both Donor and Acceptor Materials for High Performance Non-Fullerene Polymer Solar Cells with 13.5% Efficiency. *Sci. China Chem.* **2018**, *61*, 531–537.

(42) Yao, H.; Cui, Y.; Yu, R.; Gao, B.; Zhang, H.; Hou, J. Design, Synthesis, and Photovoltaic Characterization of a Small Molecular Acceptor with an Ultra-Narrow Band Gap. *Angew. Chemie - Int. Ed.* **2017**, *56*, 3045–3049.

(43) Jo, J.; Na, S.I.; Kim, S.S.; Lee, T.W.; Chung, Y.; Kang, S.J.; Vak, D.; Kim, D.Y. Three-Dimensional Bulk Heterojunction Morphology for Achieving High Internal Quantum Efficiency in Polymer Solar Cells. *Adv. Funct. Mater.* **2009**, *19*, 2398–2406.

(44) Oosterhout, S.D.; Wienk, M.M.; VanBavel, S.S.; Thiedmann, R.; Jan Anton Koster, L.; Gilot, J.; Loos, J.; Schmidt, V.; Janssen, R.A.J. The Effect of Three-Dimensional Morphology on the Efficiency of Hybrid Polymer Solar Cells. *Nat. Mater.* **2009**, *8*, 818-824.

(45) Li, W.; Cai, J.; Yan, Y.; Cai, F.; Li, S.; Gurney, R.S.; Liu, D.; McGettrick, J.D.; Watson, T. M.; Li, Z.; Pearson, A.J.; Lidzey, D.J.; Hou, J.; Wang, T. Correlating Three-Dimensional Morphology With Function in PBDB-T:IT-M Non-Fullerene Organic Solar Cells. *Sol. RRL.* **2018**, *2*, 1800114.

(46) Qian, D.; Zheng, Z.; Yao, H.; Tress, W.; Hopper, T.R.; Chen, S.; Li, S.; Liu, J.; Chen, S.; Zhang, J.; Liu, X.; Gao, B.; Ouyang, L.; Jin, Y.; Pozina, G.; Buyanova, I.A.; Chen ,W.;

Inganäs, O.; Coropceanu, V.; Bredas, J.; Yan, H.; Hou, J.; Zhang, F.; Bakulin, A.A.; Gao, F. Design Rules for Minimizing Voltage Losses in -Efficiency Organic Solar Cells. *Nat. Mater.* **2018**, *17*, 703-709.

(47) Li, S.; Ye, L.; Zhao, W.; Liu, X.; Zhu, J.; Ade, H.; Hou, J. Design of a New Small-Molecule Electron Acceptor Enables Efficient Polymer Solar Cells with High Fill Factor. *Adv. Mater.* **2017**, *29*, 1704051.

(48) Fei, Z.; Eisner, F. D.; Jiao, X.; Azzouzi, M.; Röhr, J. A.; Han, Y.; Shahid, M.; Chesman, A.S.; Easton, C.D.; McNeill.; C.R.; Anthopoulos, D.R.; Nelson, J.; Heeney, M. An Alkylated Indacenodithieno[3,2-b]Thiophene-Based Nonfullerene Acceptor with High Crystallinity Exhibiting Single Junction Solar Cell Efficiencies Greater than 13% with Low Voltage Losses. *Adv. Mater.* **2018**, *30*, 1705209.

(49) Mai, J.; Xiao, Y.; Zhou, G.; Wang, J.; Zhu, J.; Zhao, N.; Zhan, X.; Lu, X. Hidden Structure Ordering Along Backbone of Fused-Ring Electron Acceptors Enhanced by Ternary Bulk Heterojunction. *Adv. Mater.* **2018**, *30*, 1802888.

(50) Song, X.; Gasparini, N.; Ye, L.; Yao, H.; Hou, J.; Ade, H.; Baran, D. Controlling Blend Morphology for Ultrahigh Current Density in Nonfullerene Acceptor-Based Organic Solar Cells. *ACS Energy Lett.* **2018**, *3*, 669–676.

(51) Ma, X.; Mi, Y.; Zhang, F.; An, Q.; Zhang, M.; Hu, Z.; Liu, X.; Zhang, J.; Tang, W. Efficient Ternary Polymer Solar Cells with Two Well-Compatible Donors and One Ultranarrow Bandgap Nonfullerene Acceptor. *Adv. Energy. Mater.* **2018**, *8*, 1702854.

(52) Wang, T.; Pearson, A. T.; Dunbar, A. D. F.; Staniec, P. A.; Watters, D. C.; Coles, D.; Yi, H.; Iraqi, A.; Lidzey. D. G.; Jones, R. A. L. Competition between Substrate-mediated π-π Stacking and Surface-mediated Tg Depression in Ultrathin Conjugated Polymer Films. *Eur. Phys. J. E*. **2012**, *35*, 129-134.

(53) Mao, Y.; Li, W.; Chen, M.; Chen, X.; Gurney, R. S.; Liu, D.; Wang, T. Evolution of Molecular Aggregation in Bar-coated Non-fullerene Organic Solar Cells. *Mater. Chem. Front.* **2019**, *3*, 1062-1070.

(54) Liu, D.; Qin, H.; Zhang, J.-H.; Wang, T. Thickness-dependent glass transition temperature and charge mobility in cross-linked polyfluorene thin films. *Phy. Rev. E.* **2016**, *94*, 0525033.

(55) Cui, Y.; Zhang, S.; Liang, N.; Kong, J.; Yang, C.; Yao, H.; Ma, L.; Hou, J. Toward Efficient Polymer Solar Cells Processed by a Solution-Processed Layer-By-Layer Approach. *Adv.*

Mater. **2018**, *30*, 1802499.

(56) Huang, L.; Wang, G.; Zhou, W.; Fu, B.; Cheng, X.; Zhang, L.; Yuan, Z.; Xiong, S.; Zhang, L.; Xie, Y.; Zhang, A.; Zhang, Y.; Ma, W.; Li, W.; Zhou, Y.; Reichmani, E.; Chen, Y. Vertical Stratification Engineering for Organic Bulk-Heterojunction Devices. *ACS Nano.* **2018**, *12*, 4440–4452.

(57) Yan, Y.; Liu, X.; Wang, T. Conjugated-Polymer Blends for Organic Photovoltaics: Rational Control of Vertical Stratification for High Performance. *Adv. Mater.* **2017**, *29*, 1601674.

(58) Li, W.; Cai, J.; Cai, F.; Yan, Y.; Yi, H.; Gurney, R.S.; Liu, D.; Iraqi, A.; Wang, T. Achieving over 11% Power Conversion Efficiency in PffBT4T-2OD-Based Ternary Polymer Solar Cells with Enhanced Open-Circuit-Voltage and Suppressed Charge Recombination. *Nano Energy.* **2018**, *44*, 155–163.

(59) Koster, L.J.A.; Mihailetchi, V.D.; Xie, H.; Blom, P.W.M. Origin of the Light Intensity Dependence of the Short-Circuit Current of Polymer/Fullerene Solar Cells. *Appl. Phys. Lett.* **2005**, *87*, 203502.

(60) Li, W.; Chen, M.; Zhang, Z.; Cai, J.; Zhang, H.; Gurney, R.S.; Liu, D.; Yu, J.; Tang, W.; Wang, T. Retarding the Crystallization of a Nonfullerene Electron Acceptor for High‐Performance Polymer Solar Cells. *Adv. Funct. Mater.* **2019**, 29, 1807662.

(61) Zheng, Y.; Goh, T.; Fan, P.; Shi, W.; Yu, J.; Taylor, A.D. Toward Efficient Thick Active PTB7 Photovoltaic Layers Using Diphenyl Ether as a Solvent Additive. *ACS Appl. Mater. Interfaces.* **2016**, *8*, 15724–15731.

(62) Clarke, T.M.; Lungenschmied, C.; Peet, J.; Drolet, N.; Mozer, A.J. A Comparison of Five Experimental Techniques to Measure Charge Carrier Lifetime in Polymer/Fullerene Solar Cells. *Adv. Energy. Mater.* **2015**, *5* , 1401345.

Table of Contents